ARTICLE

Ambient-pressure hydrogenation of CO_2 into long-chain olefins

Zhongling Li[1,4], Wenlong Wu[1,4], Menglin Wang[1], Yanan Wang[2,3], Xinlong Ma[1], Lei Luo[1], Yue Chen[1], Kaiyuan Fan[1], Yang Pan[1], Hongliang Li ●[1✉] & Jie Zeng ●[1✉]

The conversion of CO_2 by renewable power-generated hydrogen is a promising approach to a sustainable production of long-chain olefins ($C_{4+}^=$) which are currently produced from petroleum resources. The decentralized small-scale electrolysis for hydrogen generation requires the operation of CO_2 hydrogenation in ambient-pressure units to match the manufacturing scales and flexible on-demand production. Herein, we report a Cu-Fe catalyst which is operated under ambient pressure with comparable $C_{4+}^=$ selectivity (66.9%) to that of the state-of-the-art catalysts (66.8%) optimized under high pressure (35 bar). The catalyst is composed of copper, iron oxides, and iron carbides. Iron oxides enable reverse-water-gas-shift to produce CO. The synergy of carbide path over iron carbides and CO insertion path over interfacial sites between copper and iron carbides leads to efficient C-C coupling into $C_{4+}^=$. This work contributes to the development of small-scale low-pressure devices for CO_2 hydrogenation compatible with sustainable hydrogen production.

[1] Hefei National Research Center for Physical Sciences at the Microscale, Key Laboratory of Strongly-Coupled Quantum Matter Physics of Chinese Academy of Sciences, National Synchrotron Radiation Laboratory, Key Laboratory of Surface and Interface Chemistry and Energy Catalysis of Anhui Higher Education Institutes, Department of Chemical Physics, University of Science and Technology of China, Hefei, Anhui 230026, PR China. [2] Songshan Lake Materials Laboratory, Dongguan, Guangdong 523808, PR China. [3] Beijing National Laboratory for Condensed Matter Physics and Institute of Physics, Chinese Academy of Sciences, Beijing 100190, PR China. [4] These authors contributed equally: Zhongling Li, Wenlong Wu. ✉email: lihl@ustc.edu.cn; zengj@ustc.edu.cn

As the culprit for greenhouse effect, CO_2, especially those in high purity released from cement manufacturing, breweries, and fuel processing facilities, can be regarded as a promising candidate to synthesize chemicals which are currently produced from fossil resources. Long-chain olefins ($C_{4+}^=$) are versatile industrial feedstocks for a variety of value-added products such as synthetic lubricants, high-octane gasoline, biodegradable detergents, new polymers, agricultural chemicals, coatings, and corrosion inhibitors[1,2]. The prevalent method for the synthesis of these olefins is based on oligomerization of ethylene which is mostly produced from petroleum resources[3,4]. The use of $C_{4+}^=$ as industrial feedstocks would play a pivotal role in the development of a sustainable society if $C_{4+}^=$ could be directly obtained from CO_2 hydrogenation. To ensure the whole process carbon negative, H_2 must be produced from water electrolysis powered by renewable energy instead of coal gasification or reforming of natural gas[5,6]. Considering that electrolysis is distributed and produced in small-scale devices, it would be attractive to perform the subsequent CO_2 hydrogenation in ambient-pressure units for matching the manufacturing scales and flexible on-demand production[7,8].

For CO_2 hydrogenation, ambient pressure is adverse to the formation of liquid long-chain olefins based on Le Chatelier's principle. Currently, olefins produced from CO_2 hydrogenation are mainly in the gaseous range of $C_{2-4}^=$, where the corresponding catalysts generally comprised metal oxides for methanol synthesis and zeolites for methanol-to-olefin process[9–11]. Limited catalysts targeting on long-chain olefins were operated under high pressure[12–14]. For instance, an iron aluminum oxide exhibited high selectivity (66.8%) for long-chain olefins ($C_{4+}^=$) under 35 bar[15]. However, it is not simply a case of lowering the pressure for these catalysts if one intends to achieve ambient-pressure synthesis of long-chain olefins.

Designing a tandem process including CO-intermediate and methanol-intermediate routes represents a successful strategy for CO_2 hydrogenation into long-chain products[16–18]. To carter to the ambient-pressure condition, we should choose CO-intermediate route because low-pressure benefits reverse-water-gas-shift (RWGS) reaction but suppresses methanol synthesis process[8]. In this regard, the challenge lies in seeking active sites for Fischer-Tropsch synthesis (FTS) under ambient pressure. C–C coupling during FTS generally includes carbide mechanism and CO insertion mechanism[19–22]. The carbide mechanism involves the dissociation of CO into surface carbon, the hydrogenation of surface carbon into CH_x^* ($x = 1$, 2, or 3) intermediates, the surface polymerization of CH_x^* (chain growth), and the hydrogenation (chain termination) to form hydrocarbon products[19]. The low total pressure induces low surface coverage of CH_x^* due to the insufficient dissociation of CO, resulting in the short-chain length and a large amount of undissociated CO molecules. If these undissociated CO molecules are utilized as the monomer unit for chain growth, namely CO insertion mechanism[21], it is promising to achieve the formation of long-chain products under ambient pressure.

Herein, we report a Cu–Fe catalyst which was operated under ambient pressure with comparable $C_{4+}^=$ selectivity to that of the state-of-the-art catalysts optimized under high pressure toward CO_2 hydrogenation (Supplementary Fig. 1 and Supplementary Table 1). The catalyst activated from delafossite oxides $CuFeO_2$ contained Cu, iron oxides, and iron carbides, which was denoted as activated $CuFeO_2$. Iron oxides enabled RWGS reaction to produce CO, while CO underwent carbide mechanism over iron carbides and experienced CO insertion over interfacial sites between copper and iron carbides. The synergy of carbide path and CO insertion path resulted in a high $C_{4+}^=$ selectivity of 66.9% (excluding CO) and a CO_2 conversion of 27.3% under

1 bar (H_2:$CO_2 = 3$:1) with a space velocity of 2400 mL h^{-1} g_{cat}^{-1} at 320 °C. Moreover, we found that increasing the total pressure (30 bar) was able to refresh the deactivated catalyst during CO_2 hydrogenation under ambient pressure.

Results and discussion

Catalytic properties. We prepared the catalysts via a hydrothermal method. The resulting sample exhibited a typical delafossite-type structure with homogeneous distribution of Cu, Fe, and O elements, which was denoted as fresh $CuFeO_2$ (Supplementary Figs. 2 and 3). The fresh $CuFeO_2$ was activated via H_2 reduction under 4 bar at 400 °C for 2 h, followed by being exposed to 1 bar of mixed gas (H_2:$CO_2 = 3$:1) with a space velocity of 2,400 mL h^{-1} g_{cat}^{-1} at 320 °C for 4 h since when the conversion of CO_2 became stable. The obtained catalyst was designated as activated $CuFeO_2$. The catalytic properties of activated $CuFeO_2$ were evaluated in a fixed-bed reactor under 1 bar (H_2:$CO_2 = 3$:1) with a space velocity of 2,400 mL h^{-1} g_{cat}^{-1} at 320 °C for 4 h on stream. The ambient pressure inevitably resulted in high CO selectivity of 43.7%. The selectivity for C_{4+} hydrocarbons was 74.0% (excluding CO) with an extremely high ratio (9.4) of olefin to paraffin (o/p ratio) at a CO_2 conversion of 27.3% (Fig. 1a and Supplementary Table 1). Though activated $CuFeO_2$ was operated under ambient pressure, the $C_{4+}^=$ selectivity was as high as 66.9%, which was comparable to that over the state-of-the-art catalysts optimized for high-pressure conversion (Supplementary Table 1). The CH_4 selectivity reached 5.4%, while the selectivity for C_{2-3} hydrocarbons was 20.6%. Figure 1b shows the distribution of hydrocarbon products, well matching the Anderson–Schulz–Flory (ASF) distribution. The probability of chain growth (α) was calculated as 0.72, while the coefficient of determination (R^2) was 0.98. As indicated by the high linearity and high CO selectivity, the reaction tandemly proceeds along a RWGS reaction and a typical FTS process obeying the ASF model. Once following ASF distribution, the carbon chain grew via one-carbon-atom process while the α value was independent on carbon numbers[23]. Notably, the hydrocarbon distribution of activated $CuFeO_2$ behaved differently from that of a similar reported catalyst even under the same condition[24] (Supplementary Table 2 and Supplementary Fig. 4). In addition, the pre-reduction in 1 bar of H_2 did no obviously influence the catalytic activity and selectivity compared with the catalyst pre-reduced in 4 bar of H_2 (Supplementary Table 3).

By comparison, Fe_2O_3 after the same activation procedure (denoted as activated Fe_2O_3) was tested under 1 bar (H_2:$CO_2 = 3$:1) with a space velocity of 2,400 mL h^{-1} g_{cat}^{-1} at 320 °C for 4 h on stream. The C_{4+} selectivity reached 46.0% (excluding CO) with an o/p ratio of 7.2 at a CO_2 conversion of 26.6%, whereas the selectivities for CH_4 and C_{2-3} hydrocarbons were 17.9% and 36.1%, respectively (Fig. 1a and Supplementary Table 1). The $C_{4+}^=$ selectivity was 40.4%, lower than that (66.9%) over activated $CuFeO_2$. As shown in Supplementary Figure 5, the distribution of hydrocarbon products for activated Fe_2O_3 also followed the ASF distribution with an α value of 0.59 and a high R^2 value of 0.99. When the total pressure increased to 30 bar, the $C_{4+}^=$ selectivity increased to 50.2% (Supplementary Table 1). In addition, we prepared ZnO-ZrO_2 solid solution supported on a Zn-modified SAPO-34 zeolite (ZnZrO/SAPO) as a reference catalyst. This catalyst was reported as a highly selective catalyst toward light olefins under high pressure[25]. Considering that ZnZrO/SAPO was active at high temperature (360–400 °C), we tested its catalytic performance under 1 bar (H_2:$CO_2 = 3$:1) with a space velocity of 2,400 mL h^{-1} g_{cat}^{-1} at 380 °C. Under this condition, the major product was light olefins (C_2–$C_4^=$) with the selectivity of 61.4% instead of long-chain olefins ($C_{4+}^=$) with the
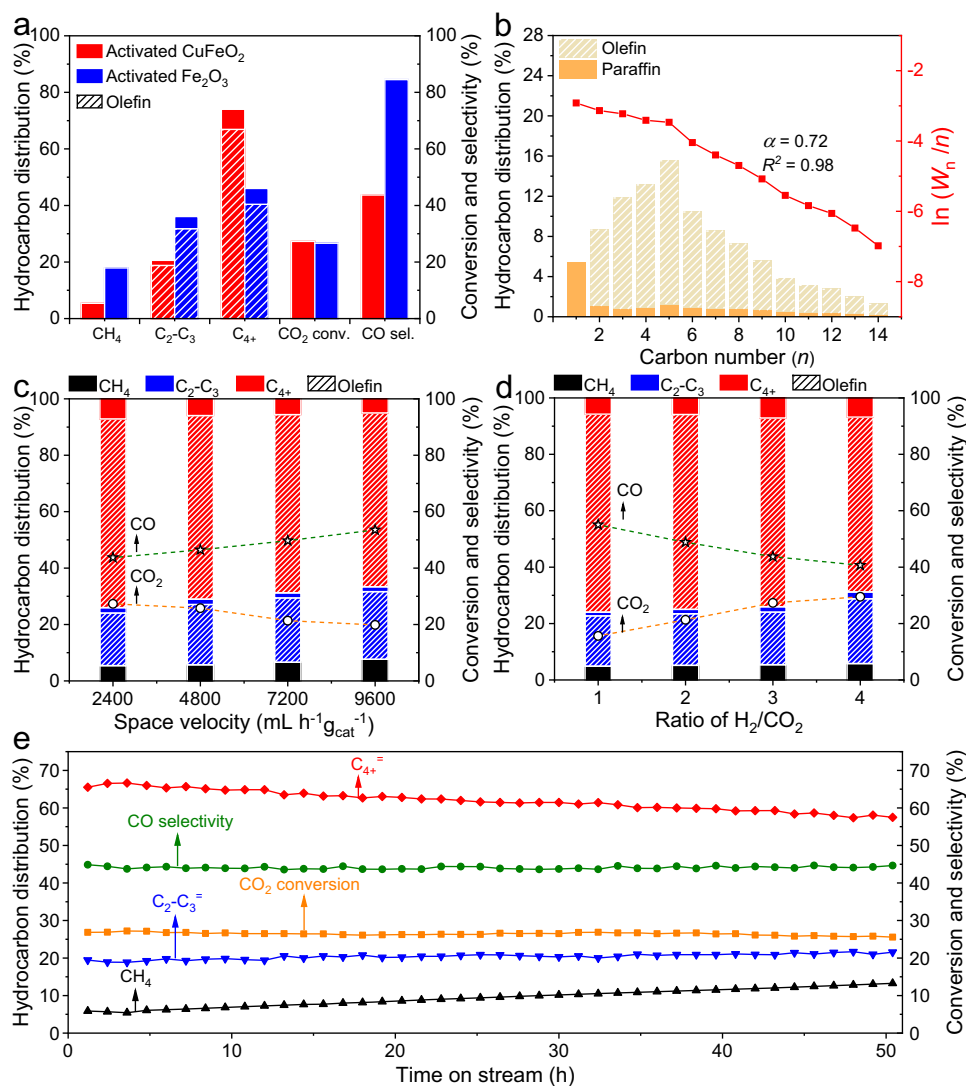
Fig. 1 Catalytic properties toward CO$_2$ hydrogenation. a The hydrocarbon product distribution, CO$_2$ conversion, and CO selectivity of activated CuFeO$_2$ and activated Fe$_2$O$_3$. **b** The detailed hydrocarbon product distribution, the ASF plot, and the corresponding α value of activated CuFeO$_2$. α is the probability of chain growth. R^2 is the coefficient of determination, describing the goodness of linear fitting. W_n is the weight fraction of a product with n carbon atoms. CO$_2$ conversion and product selectivity at **c** different space velocities and **d** different H$_2$:CO$_2$ ratios over activated CuFeO$_2$. **e** Stability test of activated CuFeO$_2$. For panels **a** and **b**, the reaction was conducted under 1 bar (H$_2$:CO$_2$ = 3:1) with a space velocity of 2400 mL h^{-1} g$_{cat}^{-1}$ at 320 °C after 4 h on stream. The reaction conditions for panels **c**–**e** are similar to that for panel **a** except for the space velocity, H$_2$:CO$_2$ ratio, and time on stream, respectively. The selectivity for hydrocarbon product excludes CO.

selectivity of 3.5% (Supplementary Table 1). Moreover, the selectivities for CO and methane (excluding CO) boosted to 85.1% and 30.3%, respectively (Supplementary Table 1), because lowering the pressure suppresses methanol synthesis due to Le Chatelier's principle.

To investigate the robustness of activated CuFeO$_2$, we varied the space velocity and the ratio of H$_2$ to CO$_2$ over activated CuFeO$_2$. When the space velocity increased from 2400 to 9600 mL h^{-1} g$_{cat}^{-1}$, the C$_{4+}$$^=$ selectivity decreased slightly from 66.9% to 61.6% (Fig. 1c). Moreover, the selectivity for CH$_4$, C$_{2-3}$, and C$_{4+}$ along with o/p ratios also exhibited slight variations, while the conversion of CO$_2$ decreased from 27.3% to 19.8% (Fig. 1c). When the ratio of H$_2$ to CO$_2$ increased from 1 to 4 with the space velocity of 2,400 mL h^{-1} g$_{cat}^{-1}$, the C$_{4+}$$^=$ selectivity dropped from 70.2% to 62.0%, while the conversion of CO$_2$ rose from 15.6% to 29.5% (Fig. 1d). Therefore, the selectivity for long-chain olefins is insensitive to both the space velocity and the ratio of H$_2$ to CO$_2$, indicating high robustness

of activated CuFeO$_2$ which applied to a wide range of reaction conditions.

We further investigated the stability of activated CuFeO$_2$ under 1 bar (H$_2$:CO$_2$ = 3:1) with a space velocity of 2,400 mL h^{-1} g$_{cat}^{-1}$ at 320 °C. After 50 h on stream, the conversion of CO$_2$ kept stable, whereas the selectivity for long-chain olefins (C$_{4+}$$^=$), unfortunately, dropped to 57.6% (Fig. 1e). Meanwhile, the selectivity for methane increased to 14.6%. Thus, activated CuFeO$_2$ was not stable enough during ambient-pressure hydrogenation of CO$_2$.

Regeneration of activated CuFeO$_2$. We notice that an elevated total pressure (30 bar) with high H$_2$:CO$_2$ ratio (3:1) enables the coverage of surface hydrogen on catalysts to become high enough for minimizing carbon formation[26,27]. Inspired by these points, we propose that increasing the total pressure serves as a promising approach to the regeneration of the catalysts. When the
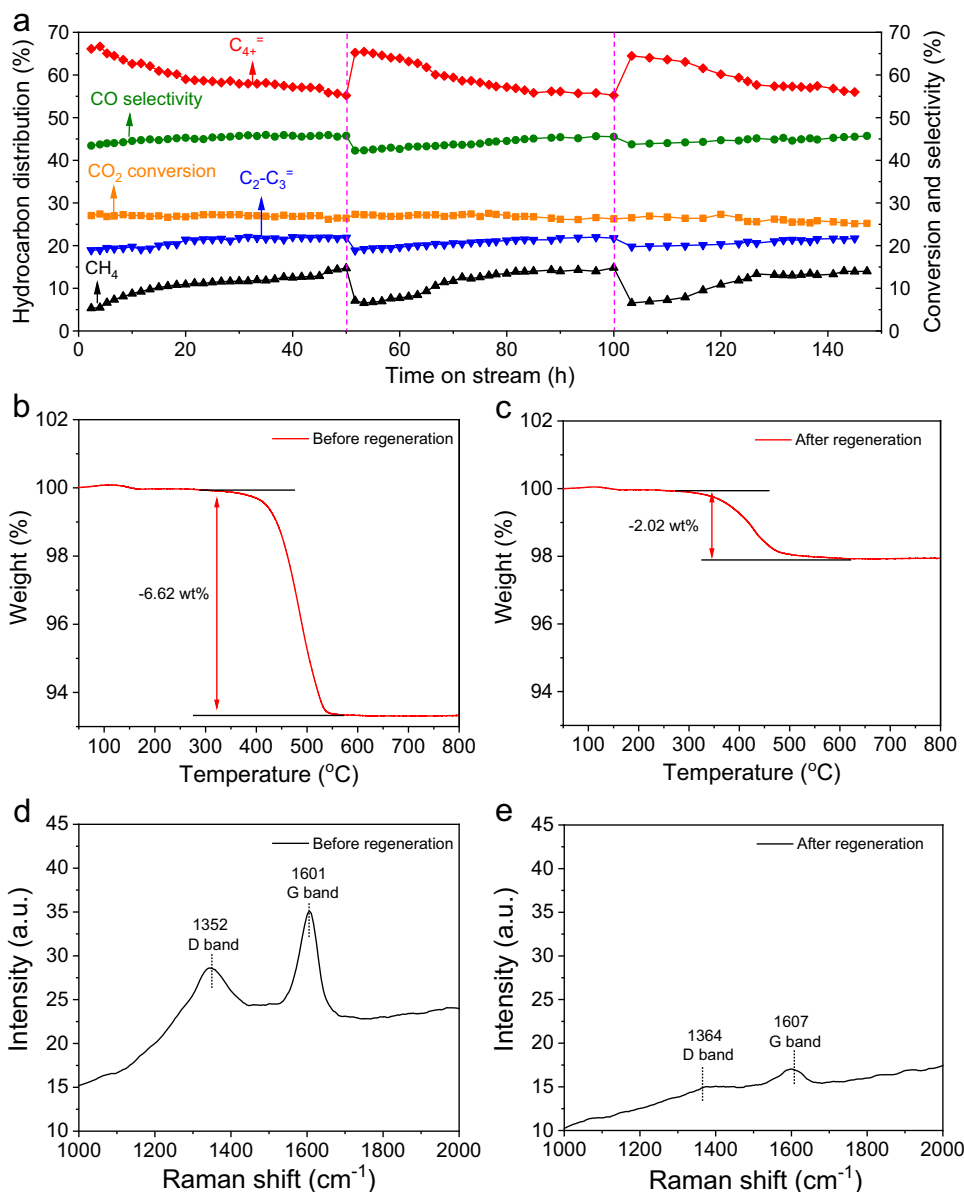
Fig. 2 Regeneration of activated CuFeO$_2$. a Long-term stability test with regeneration over activated CuFeO$_2$. The reaction was conducted under 1 bar (H$_2$:CO$_2$ = 3:1) with a space velocity of 2400 mL h^{-1} g$_{cat}^{-1}$ at 320 °C. The purple dash vertical lines refer to the regeneration treatment that was conducted under 30 bar (H$_2$:CO$_2$ = 3:1) with a space velocity of 2400 mL h^{-1} g$_{cat}^{-1}$ at 320 °C for 4 h on stream. TGA profiles of activated CuFeO$_2$ **b** before regeneration treatment and **c** after regeneration treatment. Raman spectra of activated CuFeO$_2$ **d** before regeneration treatment and **e** after regeneration treatment.

reaction proceeded under 1 bar at 320 °C for 50 h on stream, the C$_{4+}^=$ selectivity declined to 55.2% (Fig. 2a). Afterward, the total pressure was increased to 30 bar. Under this condition, the C$_{4+}^=$ selectivity reached 66.3% under 30 bar, almost equal to that (66.9%) under ambient pressure (Supplementary Table 3). Compared with the results obtained under 1 bar, the major difference lies in the significant decrease of CO selectivity (12.3%) and the appearance of oxygenated products with the selectivity of 7.5% (Supplementary Table 3). Based on Le Chatelier's principle, the elevated pressure promotes the conversion of CO to hydrocarbons and oxygenated products, while RWGS is insensitive to pressure, accounting for the decreased selectivity for CO. The appearance of oxygenated products indicates the existence of CO insertion mechanism in the catalytic system[21]. After operating the catalyst under 30 bar for 4 h, we lowered the total pressure back to 1 bar. It is worth noting that the C$_{4+}^=$ selectivity recovered to

65.2% (Fig. 2a). When we repeated the regeneration procedure, activated CuFeO$_2$ resumed its high selectivity for C$_{4+}^=$ every time. Therefore, elevating the total pressure represents a convenient regeneration method which does not need to switch gases or unload the catalysts from the reactor.

The effect of the regeneration was investigated by means of thermogravimetric analysis (TGA) in N$_2$ atmosphere. For activated CuFeO$_2$ that had been operated under 1 bar for 50 h (denoted as the catalyst before regeneration), the weight was lost by 6.62 wt% (Fig. 2b). The catalyst after working under 1 bar for 50 h and subsequently under 32 bar for 4 h was denoted as the catalyst after regeneration. During TGA tests, activated CuFeO$_2$ after regeneration lost 2.02 wt% weight, which was lower than that (6.62 wt%) before regeneration (Fig. 2c). As such, high-pressure treatment cleaned long-chain hydrocarbons to refresh the catalyst. We further conducted Raman measurements. The

peaks at 1352 and 1364 cm^{-1} were assigned to disordered carbon (D band), while those at 1601 and 1607 cm^{-1} corresponded to graphite (G band) (Fig. 2d, e)[28]. The intensities of these two peaks for activated CuFeO$_2$ before regeneration were higher than those for the catalyst after regeneration (Fig. 2d, e). In this case, high-pressure treatment is also able to remove disordered carbon and graphite.

In addition, we conducted Brunauer–Emmett–Teller (BET) measurements of activated CuFeO$_2$ after different treatments. For clarity, we denote samples I, II, III, and IV as the activated CuFeO$_2$ after reaction for 0, 10, 20 h, and regeneration, respectively. The BET surface areas of samples I, II, III, and IV were measured as 2.88, 2.62, 2.35, and 2.96 m^2 g^{-1}, respectively (Supplementary Fig. 6). In this case, the BET surface area decreased with the prolonged reaction time and recovered after regeneration. However, the variation in surface area of the samples after different treatments was not prominent, presumably consistent with the stable conversion of CO$_2$. There must be other underlying mechanisms for catalyst deactivation and regeneration in addition to carbon deposition. To this end, we conducted energy dispersive X-ray (EDX) elemental mapping characterizations of samples I, III, and IV. We found that the spatial overlap between Cu and Fe elements of sample III is obviously smaller than that of sample I and that of sample IV (Supplementary Figs. 7–9). As such, we speculate that the deactivation and regeneration are presumably associated with the segregation and re-dispersion of Cu and Fe elements.

Structural and electronic characterizations of activated CuFeO$_2$. To explore the nature of active sites, we resorted to multiple structural characterizations. Comparing scanning electron microscopy (SEM) images of fresh and activated CuFeO$_2$, we found that the activation procedure etched the initial polyhedral particles into a porous structure (Supplementary Figs. 2a and 10). Figure 3a shows a high-angle annular dark-field scanning transmission electron microscopy (HAADF-STEM) image of activated CuFeO$_2$. The lattice parameters of 0.21, 0.25, and 0.22 nm were ascribed to Cu(111), Fe$_3$O$_4$(311), and χ-Fe$_5$C$_2$(11-2) facets,

respectively. The interfaces between these facets marked by red lines were clearly identified. Supplementary Figure 7a shows EDX elemental mapping images, suggesting that activated CuFeO$_2$ comprised Cu, Fe, O, and C elements. In comparison with the elemental mapping images of fresh CuFeO$_2$, the compositional line profile of activated CuFeO$_2$ indicated that the homogeneously distributed Cu and Fe elements underwent obvious segregation after the activation (Supplementary Fig. 7b). Moreover, the activation treatment led to intimate contact between Cu and Fe species as indicated by elemental mapping images and compositional line profile (Supplementary Fig. 7). The phase segregation was further verified by the X-ray diffraction (XRD) profile of activated CuFeO$_2$. As shown in Fig. 3b, the characteristic XRD peaks were assigned to the phases of Hägg carbides (χ-Fe$_5$C$_2$) and pure Cu. The Mössbauer spectra of activated CuFeO$_2$ showed that iron phases include χ-Fe$_5$C$_2$, Fe$_3$C, and Fe$_3$O$_4$. Specially, χ-Fe$_5$C$_2$, Fe$_3$C, and Fe$_3$O$_4$ occupied 73.6%, 9.8%, and 16.6% of the total iron phases (Fig. 3c and Supplementary Table 4). The iron phases of activated CuFeO$_2$ were different from those of a similar reported catalyst which contained metallic Fe and χ-Fe$_5$C$_2$ without iron oxides[24]. In comparison, the structures of activated Fe$_2$O$_3$ were also investigated by means of multiple characterization techniques including SEM, XRD, and Mössbauer spectroscopy. We found that activated Fe$_2$O$_3$ comprised Fe$_3$O$_4$ and χ-Fe$_5$C$_2$ (Supplementary Fig. 11 and Supplementary Table 5).

The electronic structures of activated CuFeO$_2$ were investigated via X-ray photoelectron spectroscopy (XPS) measurements. Supplementary Figure 12 shows Cu 2p XPS spectra of fresh and activated CuFeO$_2$. No evident satellite peaks were presented, indicating the absence of Cu^{2+}. However, the assignment of Cu^0 and Cu$^+$ cannot be concluded only from XPS results since Cu and Cu$^+$ have close binding energies[29,30]. To discriminate between Cu^0 and Cu$^+$, we turned to Cu *LMM* Auger measurements. The Auger spectrum of fresh CuFeO$_2$ showed a peak at 917.0 eV which arose from Cu$^+$ (Fig. 3d)[29,30]. As for activated CuFeO$_2$, two peaks at 916.6 and 918.7 eV were observed, corresponding to Cu$^+$ and Cu^0, respectively (Fig. 3d)[29,30]. Based on Fe 2p XPS spectra, Fe species on fresh CuFeO$_2$ were at the oxidation state of +3, whereas activated
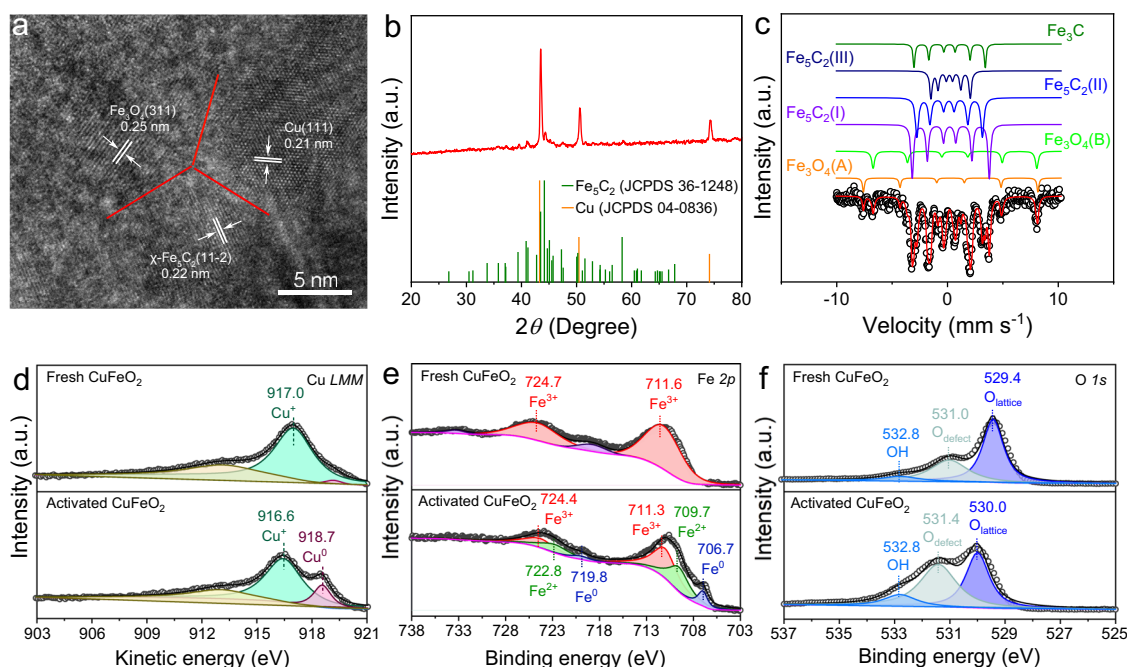

Fig. 3 Structural characterizations of activated CuFeO$_2$. a HAADF image of activated CuFeO$_2$. **b** XRD profiles of activated CuFeO$_2$. **c** Mössbauer spectra of activated CuFeO$_2$. **d** Cu *LMM* Auger, **e** Fe 2p XPS, and **f** O 1s XPS spectra of fresh and activated CuFeO$_2$.

$CuFeO_2$ contained Fe^{3+}, Fe^{2+}, and Fe^0 species (Fig. 3e)[31,32]. As shown in Fig. 3f, O $1s$ spectra were deconvoluted into three peaks. Specially, the main peaks at around 529.4 and 530.0 eV were ascribed to the lattice O atoms ($O_{lattice}$)[9,33]. The peaks at 531.0 and 531.4 eV were assigned to O atoms proximal to a defect (O_{defect}), while those at 532.8 eV corresponded surface hydroxyl groups (OH^*)[9,33].

Based on structural and electronic characterizations, we conclude how $CuFeO_2$ reconstructed after the activation procedure. After the activation, Cu^+ in the lattice of $CuFeO_2$ collapsed and aggregated to form pure Cu phase with partially oxidized surface. Meanwhile, Fe^{3+} in the lattice of $CuFeO_2$ underwent partial reduction and carbonization, resulting in the formation of Fe_3O_4, χ-Fe_5C_2, and Fe_3C. In this case, a mixed states of Fe^{3+}, Fe^{2+}, and Fe^0 existed. Therefore, activated $CuFeO_2$ was composed of copper, iron oxides, and iron carbides. Moreover, these species were in intimate contact with each other, resulting in the formation of multiple interfacial sites such as the interface between Cu and χ-Fe_5C_2.

Mechanistic studies. In order to explore the origin of high selectivity for $C_{4+}^=$ olefins under ambient pressure, we conducted temperature-programmed desorption (TPD) measurements to explore the adsorption of CO. Specially, the samples were exposed to the mixed gas (CO:He = 1:9) under 1 bar at 50 °C for 30 min, followed by being purged in He for 30 min. The TPD curves were recorded from 50 °C to 800 °C at a heating rate of 5 °C min^{-1}. The CO-TPD profile of activated Fe_2O_3 shows a peak at 508 °C for dissociative adsorption of CO (Fig. 4a)[34]. Considering that activated Fe_2O_3 comprised Fe_3O_4 and χ-Fe_5C_2, we proposed the reaction scheme of activated Fe_2O_3 as that for Fe-based catalysts previously reported[16,35,36]. Specially, CO_2 was hydrogenated over Fe_3O_4 into CO via RWGS, while the produced CO was dissociated on χ-Fe_5C_2 and subsequently underwent FTS process to yield product whose distribution followed ASF distribution. As for the CO-TPD profile of activated $CuFeO_2$, two peaks at 290 and 501 °C appeared, corresponding to non-dissociative and dissociative adsorption of CO, respectively (Fig. 4a)[34,37]. The non-dissociative adsorption of CO^* was further supported by diffuse reflectance infrared Fourier transform spectroscopy (DRIFTS) measurements using CO as a probe molecule. Compared with the DRIFTS spectrum of activated Fe_2O_3, the DRIFTS spectrum of activated $CuFeO_2$ showed an additional peak at 2061 cm^{-1} (Supplementary Fig. 13). This peak was assigned to non-dissociative adsorption of CO^*. We further conducted in-situ DRIFTS measurements of activated $CuFeO_2$ after exposure to the mixed gas (H_2:CO_2 = 3:1, 1 bar) at 300 °C. As shown in Supplementary Fig. 14, the peaks for CH_x, gaseous CO_2, gaseous CO, and chemically adsorbed CO^* were observed. These spectroptic evidences prove non-dissociative adsorption of CO^* which serves as a prerequisite for CO insertion.

As activated $CuFeO_2$ was composed of Cu, Fe_3O_4, χ-Fe_5C_2, and Fe_3C, Fe_3O_4 enabled RWGS reaction to produce CO, while CO was non-dissociatively adsorbed on Cu and dissociatively adsorbed on iron carbides, subsequently experiencing FTS process. It is worth noting that the chain propagation process during FTS generally involves CO insertion and carbide mechanism, though all the possible mechanisms can result in the selectivity as predicted by ASF model[38]. Dissociative adsorption of CO favors carbide mechanism which is generally obeyed by C-C coupling over iron carbides[38]. Non-dissociative adsorption of CO allows for CO insertion mechanism, which is implied by the appearance of detectable oxygenated products under high pressure (Supplementary Table 3)[38].

To identify the existence of CO insertion mechanism, we resorted to probing oxygenate intermediates which are regarded as characteristics of CO insertion, because carbide mechanism cannot account for the formation of oxygenate products via surface polymerization of CH_x[39]. To detect the intermediate, we conducted synchrotron-based vacuum ultraviolet photoionization mass spectrometry (SVUV-PIMS). This technique is highly sensitive to low-concentration intermediates and able to identify isomers because of tunable photon energy and soft ionization[40,41]. The reaction proceeded under 1 bar (H_2:CO_2 = 3:1) with a high space velocity of 36,000 mL h^{-1} g$_{cat}^{-1}$ at 320 °C to shorten the contact time in case that active intermediates would be hydrogenated. The photon energy was selected at 10.40 eV to avoid the ionization of CO_2 whose ionization energy is 13.77 eV[42]. For activated $CuFeO_2$, a signal of mass/charge ratio (m/z) = 44 appeared in addition to stable hydrocarbon products (Supplementary Fig. 15). When the photon energy was varied from 9.10 to 10.40 eV, the point of inflection appeared at 10.25 eV which was assigned to acetaldehyde (CH_3CHO) after excluding the possibilities of other species with m/z = 44 (Fig. 4b and Supplementary Table 6)[43]. To investigate whether C-C coupling occurs via acetaldehyde oligomerization, we conducted temperature-programmed surface reaction (TPSR) measurements of activated $CuFeO_2$. Specially, the acetaldehyde vapor was introduced via bubbling with the mixed gas (H_2:Ar = 1:9, 1 bar) with a gas-flow rate of 100 mL min^{-1}. Then the temperature was raised to 300 °C with a rate of 10 °C min^{-1} and kept at 300 °C. During the whole period, no detectable products were observed as shown in Supplementary Fig. 16, thereby excluding the possibility of the acetaldehyde oligomerization. Therefore, we speculate that CO insertion occurred during the chain growth over activated $CuFeO_2$.

Generally, interfacial sites between copper and iron carbides are regarded as the active center for CO insertion. To gain theoretical insights into the mechanisms, we conducted density functional theory (DFT) calculations. To simulate the interface between iron carbides and copper, we established χ-Fe_5C_2 clusters on the surface of Cu(111) (Supplementary Fig. 17). This simplified model captures the main features of the interface, though this model cannot completely reproduce the real catalyst. Cu(111) and χ-Fe_5C_2(11-2) were constructed for comparison (Supplementary Fig. 17). We calculated the d-band centers of these facets to qualitatively evaluate the catalytic performance. The d-band center of Cu-χ-Fe_5C_2 interfacial sites is −0.32 eV, which is closer to the Fermi level than that (−0.69 eV) of χ-Fe_5C_2(11-2) and that (−2.02 eV) of Cu(111) facets (Supplementary Fig. 18). The upward shift of d-band center empties more antibonding states which allows for accepting more electrons from CO and alkyl species, thereby facilitating CO insertion into alkyl species[44,45].

To further investigate CO insertion over different surfaces, we calculated the energy barriers of C–C coupling. FTS is a complex process involving various possible steps. For simplicity, we use CH_2 + CO to represent the C-C coupling via CO insertion, while CH_2 + CH_2 represents the carbide mechanism. CO insertion over χ-Fe_5C_2(11-2) is an endothermic process (ΔH = + 0.48 eV), requiring an energy barrier as high as 1.61 eV (Fig. 4c and Supplementary Fig. 19). As for Cu-χ-Fe_5C_2 interfacial sites, CO insertion becomes exothermic (ΔH = −0.52 eV), while the energy barrier decreases to 0.72 eV (Fig. 4c and Supplementary Fig. 20). As such, Cu-χ-Fe_5C_2 interface significantly promotes CO insertion relative to iron alone. In contrast, the carbide mechanism is less sensitive to interface than CO insertion, as the introduction of interface only lowers the energy barrier by 0.25 eV (versus 0.89 eV in CO insertion) (Fig. 4c, d, Supplementary Figs. 19–22).
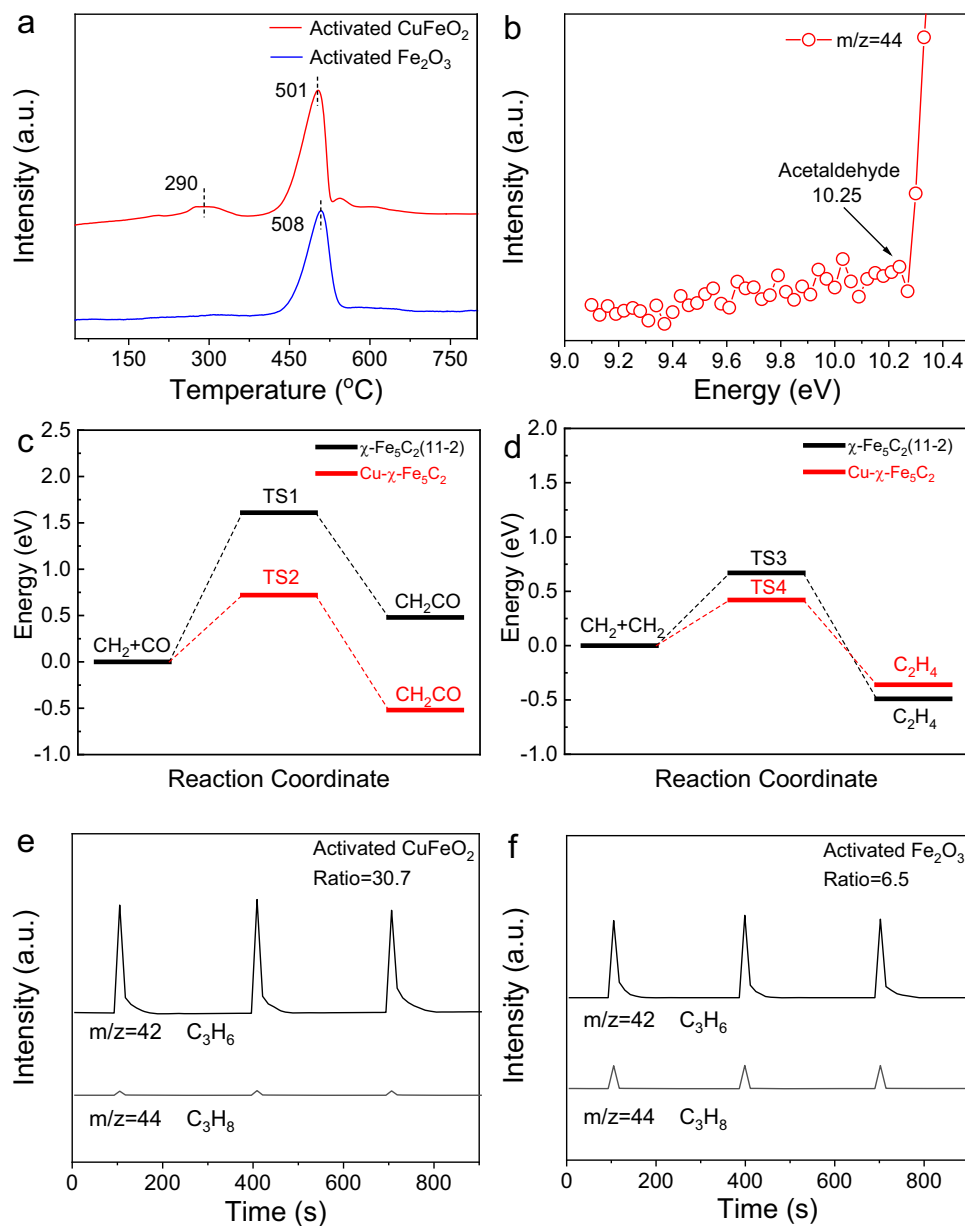
Fig. 4 Mechanistic studies. a CO-TPD profiles of activated $CuFeO_2$ and activated Fe_2O_3. **b** Absolute photoionization cross sections for acetaldehyde over activated $CuFeO_2$. **c** Comparison in energy barriers of $CH_2 + CO$ over Cu-χ-Fe_5C_2 and χ-$Fe_5C_2(11\text{-}2)$ facets. **d** Comparison in energy barriers of $CH_2 + CH_2$ over Cu-χ-Fe_5C_2 and χ-$Fe_5C_2(11\text{-}2)$ facets. Transient response curves obtained during propene pulses into H_2 flow over **e** activated $CuFeO_2$ and **f** activated Fe_2O_3. Ratio refers to the ratio of C_3H_6/C_3H_8 peak area detected by mass spectroscopy.

To support the important role played by interface, we qualitatively tuned the interfacial sites by varying the ratios of Cu to Fe from 1:9 to 9:1 in Cu-Fe binary oxides. Though we cannot quantify the interfacial sites, the amount of interfacial sites should exhibit a volcano-type trend maximized at Cu:Fe = 1:1 based on rough estimation. The reaction was conducted under 1 bar (H_2:CO_2 = 3:1) with a space velocity of 2,400 mL h^{-1} g$_{cat}$$^{-1}$ at 320 °C after 4 h on stream. As shown in Supplementary Figure 23, the selectivity for C_{4+}= exhibited a volcano-type trend against the Cu:Fe ratios with the maximum at Cu:Fe = 1:1 (activated $CuFeO_2$). We can draw a qualitative conclusion that the C_{4+}= selectivity increased with Cu-Fe interfacial sites. This result indirectly supported our claim that interfacial sites promoted C-C coupling. Therefore, the synergy of carbide path over iron carbides and CO insertion path over copper/iron carbides interfacial sites led to efficient C-C coupling

into long-chain products under ambient pressure (Supplementary Fig. 24).

Given that Cu–Fe interfacial sites contribute to C–C coupling, we explain the deactivation and regeneration mechanisms. The overlap between Cu and Fe elements can roughly estimate the amount of interfacial sites. The results show that the 20-h reaction under ambient pressure led to a significant decrease in the interfacial sites between copper and iron. Moreover, the regeneration treatment redispersed Cu and Fe elements, leading to the recovery of interfacial sites. As such, the decreased C_{4+} selectivity with the reaction time presumably derived from the decreased interfacial sites. The regeneration not only cleaned the carbon deposits but also recovered the interfacial sites, inducing the recovery of the C_{4+} selectivity.

To explain the high o/p ratio of activated $CuFeO_2$, we turned to pulse experiments for exploring whether alkenes prefer

desorption or hydrogenation on the catalysts. The catalysts were operated under 1 bar ($H_2:CO_2 = 3:1$) at 320 °C for 1 h, before switching to a H_2 flow. Afterward, propene which was chosen as the representative of alkenes was pulsed into the reactor. As shown in Fig. 4e, f, the ratio of C_3H_6/C_3H_8 peak area for activated $CuFeO_2$ was 30.7, much higher than that (6.5) for activated Fe_2O_3. Such a high ratio for activated $CuFeO_2$ indicates that the formation of propane was almost totally inhibited.

In conclusion, we achieved ambient-pressure hydrogenation of CO_2 into long-chain olefins over activated $CuFeO_2$. The $C_{4+}^=$ selectivity under 1 bar at 320 °C reached as high as 66.9% which was comparable to that of the state-of-the-art catalysts optimized under high pressure (35 bar). The high $C_{4+}^=$ selectivity under ambient pressure derives from the synergy of carbide path and CO insertion path. Our findings represent a promising approach to CO_2 conversion connected with a decentralized use of renewable power-generated hydrogen. Moreover, we offer a viable method for the regeneration of deactivated catalysts under ambient-pressure hydrogenation of CO_2.

Methods

Chemicals and materials. $Fe(NO_3)_3·9H_2O$, $Cu(NO_3)_2·3H_2O$, NaOH, Na_2CO_3, $(NH_4)_2CO_3$, $Zn(NO_3)_2·6H_2O$, $Zr(NO_3)_2·5H_2O$ and $FeCl_3$ were analytical grade and purchased from Sinopharm Chemical Reagent Co., Ltd. $FeCl_2·4H_2O$ and acetaldehyde aqueous solution (35%) were purchased from Sigma-Aldrich. SAPO-34 zeolites was purchased from Nankai University Catalyst Co., Ltd.

Synthesis of $CuFeO_2$. $CuFeO_2$ was synthesized via a hydrothermal method. Typically, 2.42 g of $Cu(NO_3)_2·3H_2O$ and 4.04 g of $Fe(NO_3)_3·9H_2O$ were added to 40 mL of deionized (DI) water with stirring to form a clear solution. In the above solution, 40 mL of 5 M NaOH aqueous solution was then added dropwise under stirring at room temperature. After stirring for 30 min, 1 mL of propionaldehyde was added as the reducing agent. The mixture was transferred to 100-mL Teflon-lined stainless steel autoclave and kept at 180 °C for 24 h. The product was separated by centrifugation, washed twice with DI water, and dried overnight at 60 °C.

Synthesis of activated $CuFeO_2$. Five hundred milligrams of $CuFeO_2$ was reduced in 4 bar of a pure H_2 flow with a flow rate of 100 mL min^{-1} at 400 °C for 2 h, followed by being exposed to 1 bar of mixed gas ($H_2:CO_2 = 3:1$) with a space velocity of 2,400 mL h^{-1} g$_{cat}^{-1}$ at 320 °C for 4 h.

Synthesis of Fe_2O_3. Fe_2O_3 was synthesized via co-precipitation method. Typically, 8.08 g of $Fe(NO_3)_3·9H_2O$ was added to 40 mL of DI water under stirring until the formation of a clear solution. In the above solution, 20 mL of 2 M Na_2CO_3 aqueous solution was then added dropwise under stirring at room temperature. After being aged for 1 h, the turbid liquid was filtrated, washed twice with DI water, and dried overnight at 60 °C. The resulting powders were calcinated in muffle furnace at 350 °C for 4 h.

Synthesis of activated Fe_2O_3. Five hundred milligrams of Fe_2O_3 was reduced in 4 bar of a pure H_2 flow with a flow rate of 100 mL min^{-1} at 400 °C for 2 h, followed by being exposed to 1 bar of mixed gas ($H_2:CO_2 = 3:1$) with a space velocity of 2,400 mL h^{-1} g$_{cat}^{-1}$ at 320 °C for 4 h.

Synthesis of ZnZrO/SAPO. ZnZrO was synthesized via co-precipitation method, Typically, 1.325 g of $Zn(NO_3)_2·6H_2O$ and 5.66 g of $Zr(NO_3)_4·5H_2O$ were dissolved in 70 mL of DI water at 70 °C. 50 mL of 0.625 M $(NH_4)_2CO_3$ aqueous solution was added dropwise under vigorous stirring at 70 °C. The pH value of the solution was kept at about 7.0. After being aged for 2 h at 70 °C, the product was separated by centrifugation, washed twice with DI water, and dried overnight at 80 °C. The resulting powders were calcinated in muffle furnace at 500 °C for 5 h. The ZnZrO/SAPO was prepared through physical mixing the ZnZrO solid solution and SAPO-34 zeolite, the mass ratio of these two components was 1:1.

Synthesis of Cu-Fe binary oxide with different ratios. copper iron binary oxide was synthesized via co-precipitation method, 2.42 g $Cu(NO_3)_2·3H_2O$ and $Fe(NO_3)_3·9H_2O$ with a given molar ratio of $Cu^{2+}:Fe^{3+}$ (9:1, 3:1, 1:3, 1:9, respectively) were dissolved in 50 mL of DI water with stirring to form a clear solution. In the above solution, 2 M Na_2CO_3 aqueous solution was then added dropwise under stirring at room temperature, and the pH value of final suspension was maintained at 9. After being aged for 1 h, the product was separated by centrifugation, washed twice with DI water, and dried overnight at 60 °C. The resulting powders were calcinated in muffle furnace at 350 °C for 4 h.

Catalytic tests. CO_2 hydrogenation reactions were carried out in a fixed-bed reactor under 1 bar of mixed gas at 320 °C. The mixed gas contained 96 vol% H_2/CO_2 as reactants and 4 vol% Ar as an internal standard. Generally, the catalyst (500 mg, 20–40 meshes) diluted with powdered quartz (500 mg, 20–40 meshes) was loaded into a fixed-bed reactor with an inner diameter of 9 mm. The catalysts refer to activated $CuFeO_2$ and activated Fe_2O_3.

For the tests over ZnZrO/SAPO, 200 mg of ZnZrO/SAPO was pretreated in an Ar flow with a flow rate of 30 mL min^{-1} at 380 °C for 1 h. Afterward, the catalyst was exposed to 1 bar of mixed gas ($H_2:CO_2 = 3:1$) with a space velocity of 2,400 mL h^{-1} g$_{cat}^{-1}$ at 380 °C. The catalytic data were obtained after when the reaction reached a steady state.

For the tests over Cu-Fe binary oxides with different ratios, 500 mg of the catalyst (20–40 meshes) was reduced in 4 bar of a pure H_2 flow with a flow rate of 100 mL min^{-1} at 400 °C for 2 h. followed by being exposed to 1 bar of mixed gas ($H_2:CO_2 = 3:1$) with a space velocity of 2,400 mL h^{-1} g$_{cat}^{-1}$ at 320 °C for 4 h.

All of the products from the reactor were introduced in a gaseous state and analyzed with two online gas chromatographs (Shimadzu GC-2014). H_2, CO, CO_2, CH_4, and Ar were analyzed by using a carbon molecular sieves column (TDX-1) with a thermal conductivity detector (TCD). Hydrocarbons were analyzed using a PONA capillary column with a flame ionization detector (FID). CH_4 was taken as a reference bridge between TCD and FID. CO_2 conversion was calculated according to an internal standard method, assuming that the amount of Ar remained constant after the reaction.

CO_2 conversion was calculated on a carbon-atom basis, as follows:

$$CO_2 \text{ conversion} = \frac{CO_{2inlet} - CO_{2outlet}}{CO_{2inlet}} \times 100\% \qquad (1)$$

where $CO_{2\ inlet}$ and $CO_{2\ outlet}$ are moles of CO_2 at the inlet and outlet, respectively.
CO selectivity was calculated according to:

$$CO \text{ selectivity} = \frac{CO_{outlet}}{CO_{2inlet} - CO_{2outlet}} \times 100\% \qquad (2)$$

where CO_{outlet} refers to moles of CO at the outlet.
The selectivity for hydrocarbon C_nH_m was obtained according to:

$$C_nH_m \text{ selectivity} = \frac{nC_nH_{m\,outlet}}{\sum_i iC_iH_{m\,outlet}} \times 100\% \qquad (3)$$

where $C_nH_{m\ outlet}$ represents moles of individual hydrocarbon product at the outlet. The selectivity for oxygenates was below 1.0% and therefore was not reported in the product selectivity. The carbon balance was over 95.0%.

Mössbauer measurements. ^{57}Fe Mössbauer spectra were carried out on a Topologic 500 A spectrometer driving with a proportional counter at room temperature. The radioactive source was ^{57}Co (Rh) moving in a constant acceleration mode. Data analyses were performed assuming a Lorentzian lineshape for computer folding and fitting.

TGA. TGA was conducted on Pyris Diamond TG-DTG in a N_2 flow with the rate of 100 mL min^{-1} at the heating rate of 5 °C min^{-1} from 50 °C to 800 °C.

CO-TPD measurements. CO-TPD measurements were conducted by using a TPD instrument (AutoChem II 2920). Prior to CO-TPD, the samples were cleaned in He with a flow rate of 50 mL min^{-1} at 200 °C for 2 h. Then, the gas was switched to the mixed gas (CO:He = 1:9, 1 bar) with a flow rate of 20 mL min^{-1} at 50 °C. After CO adsorption for 30 min, the samples were purged by He with a flow rate of 50 mL min^{-1} at 50 °C for 30 min. The CO-TPD curves were recorded from 50 °C to 800 °C at a heating rate of 5 °C min^{-1}.

DRIFTS spectra using CO as a probe molecule. In-situ DRIFTS experiments were conducted in an elevated-pressure cell (DiffusIR Accessory PN 041-10XX) with a Fourier transform infrared spectrometer (TENSOR II Sample Compartment) and a liquid-nitrogen-cooled MCT detector. Spectra were measured by accumulating 32 scans at a resolution of 8 cm^{-1}. Prior to the test, the sample was flushed with He with a gas-flow rate of 30 mL min^{-1} at 200 °C for 30 min, followed by cooling to 25 °C. The background spectra of the sample were acquired under He flow at 25 °C. Then, 1 bar (CO:He = 1:9) with a gas-flow rate of 10 mL min^{-1} was allowed to flow into the cell at 25 °C for 30 min. The spectra were recorded under the mixed gas (CO:He = 1:9).

In-situ DRIFTS spectra of activated $CuFeO_2$. In-situ DRIFTS experiments were conducted in an elevated-pressure cell (DiffusIR Accessory PN 041-10XX) with a Fourier transform infrared spectrometer (TENSOR II Sample Compartment) and a liquid-nitrogen-cooled MCT detector. Spectra were measured by accumulating 32 scans at a resolution of 8 cm^{-1}. Prior to the test, the sample was reduced in 1 bar of H_2 with a gas-flow rate of 50 mL min^{-1} at 300 °C for 30 min. Afterward, the sample was flushed with He with a gas-flow rate of 30 mL min^{-1} at 300 °C for 30 min. The background spectra of the sample were acquired under He flow at 300 °C. Then, 1 bar ($H_2:CO_2 = 3:1$) with a gas-flow rate of 20 mL min^{-1} was

allowed to flow into the cell at 300 °C for 30 min, followed by purged with 1 bar of He with a gas-flow rate of 30 mL min^{-1} at 300 °C and the spectra were obtained to detect the adsorbed species on the sample.

SVUV-PIMS. SVUV-PIMS study was carried out at the combustion beamline of the National Synchrotron Radiation Laboratory at Hefei, China. A quartz reactor with a nozzle size of ~0.1 mm was designed, which was connected to the online SVUV-PIMS spectrometer. The detection limit of SVUV-PIMS is 0.1 ppm for CO_2. The reaction proceeded under 1 bar (H_2:CO_2 = 3:1) with a space velocity of 36,000 mL h^{-1} g$_{cat}$$^{-1}$ at 320 °C.

TPSR measurement of activated $CuFeO_2$. TPSR measurement was carried out in a AutoChem II 2920 apparatus with a mass spectrometer (Hiden HPR20). The activated $CuFeO_2$ (500 mg, 20–40 meshes) was loaded in a quartz U-tube. After pretreatment with He at 200 °C for 30 min, the acetaldehyde vapor was introduced by bubbling with 1 bar (H_2:Ar = 1:9) with a gas-flow rate of 100 mL min^{-1}. Then the temperature was raised to 300 °C with a rate of 10 °C min^{-1} and kept at 300 °C.

DFT methods. DFT calculations were performed using the Vienna ab initio Simulation Package code[46-48]. The Perdew-Burke-Ernzerhof functional with generalized gradient approximation[49] was used for the geometry optimizations and electronic structure calculations. The projector-augmented wave method[50] was used to describe the electron-ion interactions. The atomic structures were fully relaxed by using a conjugate gradient scheme without symmetry restrictions until the maximum force on each atom was less than 0.02 eV Å^{-1}. A vacuum space of ~20 Å along the z direction was used to separate the interactions between the neighboring slabs with an energy cutoff of 500 eV. The Cu(111) surface containing 96 Cu atoms is simulated by using a (4 × 6) supercell (10.224 Å × 13.281 Å) with four Cu layers, where the lower two layers are fixed to the bulk structure, while the upper two layers are fully relaxed. The DFT calculated lattice constants of bulk χ-Fe_5C_2 are (a = 11.354 Å, b = 4.413 Å, c = 4.914 Å; α = γ = 90º, β = 97.61º). The χ-Fe_5C_2(11-2) surface is simulated using a (1 × 1) supercell which contains 80 Fe and 32 C atoms. The Cu-χ-Fe_5C_2 interface is constructed from a (4 × 6) Cu(111) surface and a cluster of $Fe_{10}C_4$. The (3 × 3 × 1) Monkhorst-Pack mesh is used to sample the Brillouin-zone for all the electronic structure calculations. The (1 × 1 × 1) k-mesh is used for the geometry optimizations.

TPD pulse experiments. TPD pulse experiments were carried out in a AutoChem II 2920 apparatus with a mass spectrometer (Hiden HPR20). 200 mg of activated catalysts were cleaned in He with a gas-flow rate of 50 mL min^{-1} at 200 °C for 2 h, followed by treated in 1 bar of mixed gas (H_2:CO_2 = 3:1) with a flow rate of 20 mL min^{-1} at 320 °C. After 1-h reaction, the gas was switched to the mixed gas (H_2:He = 1:9) with a flow rate of 50 mL min^{-1}. 525 µL of diluted (C_3H_6:He = 1:9) was pulsed into the system every 5 min.

Characterizations. XRD patterns were recorded by using a Philips X'Pert Pro Super diffractometer with Cu-Kα radiation (λ = 1.54178 Å). XPS measurements were conducted on an ESCALAB 250 (Thermo-VG Scientific, USA) with an Al Kα X-ray source (1486.6 eV protons) in Constant Analyser Energy (CAE) mode with pass energy of 30 eV for all spectra. The values of binding energies were calibrated with the C1s peak of contaminant carbon at 284.60 eV. Raman spectra were detected by a Renishaw. RM3000 Micro-Raman system with a 514.5 nm Ar laser.

Data availability
The data generated in this study are provided in the Supplementary Information/Source Data file. Source data are provided with this paper.

References
1. Corma, A. Inorganic solid acids and their use in acid-catalyzed hydrocarbon reactions. *Chem. Rev.* **95**, 559–614 (1995).
2. Keim, W. Oligomerization of ethylene to α-olefins: discovery and development of the shell higher olefin process (SHOP). *Angew. Chem. Int. Ed.* **52**, 12492–112496 (2013).
3. Moussa, S., Concepción, P., Arribas, M. A. & Martínez, A. Nature of active nickel sites and initiation mechanism for ethylene oligomerization on heterogeneous Ni-beta catalysts. *ACS Catal.* **8**, 3903–3912 (2018).
4. Gollwitzer, A., Dietel, T., Kretschmer, W. P. & Kempe, R. A broadly tunable synthesis of linear α-olefins. *Nat. Commun.* **8**, 1226 (2017).
5. Shih, C. F., Zhang, T., Li, J. & Bai, C. Powering the future with liquid sunshine. *Joule* **2**, 1925–1949 (2018).
6. Li, H., Zhao, J., Luo, L., Du, J. & Zeng, J. Symmetry-breaking sites for activating linear carbon dioxide molecules. *Acc. Chem. Res.* **54**, 1454–1464 (2021).
7. Luna, P. D. et al. What would it take for renewably powered electrosynthesis to displace petrochemical processes? *Science* **364**, 6438–3506 (2019).
8. Studt, F. et al. Discovery of a Ni-Ga catalyst for carbon dioxide reduction to methanol. *Nat. Chem.* **6**, 320–324 (2014).
9. Gao, P. et al. Direct production of lower olefins from CO_2 conversion via bifunctional catalysis. *ACS Catal.* **8**, 571–578 (2018).
10. Liu, X. et al. Selective transformation of carbon dioxide into lower olefins with a bifunctional catalyst composed of $ZnGa_2O_4$ and SAPO-34. *Chem. Commun.* **54**, 140–143 (2018).
11. Dang, S. et al. Role of zirconium in direct CO_2 hydrogenation to lower olefins on oxide/zeolite bifunctional catalysts. *J. Catal.* **364**, 382–393 (2018).
12. Zhang, C. et al. Uncovering the electronic effects of zinc on the structure of Fe_5C_2-ZnO catalysts for CO_2 hydrogenation to linear α-olefins. *Appl. Catal. B: Environ.* **295**, 120287 (2021).
13. Guo, L. et al. Selective formation of linear-alpha olefins (LAOs) by CO_2 hydrogenation over bimetallic Fe/Co-Y catalyst. *Catal. Commun.* **130**, 105759 (2019).
14. Wang, S. et al. Iron-potassium on single-walled carbon nanotubes as efficient catalyst for CO_2 hydrogenation to heavy olefins. *ACS Catal.* **10**, 6389–6401 (2020).
15. Kashif, K. M. et al. Selective conversion of carbon dioxide into liquid hydrocarbons and long-chain α-olefins over Fe-amorphous AlO_x bifunctional catalysts. *ACS Catal.* **10**, 10325–10338 (2020).
16. Wei, J. et al. Directly converting CO_2 into a gasoline fuel. *Nat. Commun.* **8**, 15174 (2017).
17. Gao, P. et al. Direct conversion of CO_2 into liquid fuels with high selectivity over a bifunctional catalyst. *Nat. Chem.* **9**, 1019–1024 (2017).
18. Ni, Y. et al. Selective conversion of CO_2 and H_2 into aromatics. *Nat. Commun.* **9**, 3457 (2018).
19. Brady, R. C. III & Pettit, R. On the mechanism of the Fischer-Tropsch reaction. The chain propagation step. *J. Am. Chem. Soc.* **103**, 1287–1289 (1981).
20. Kirste, B. & Kurreck, H. Reactions of diazomethane on transition-metal surfaces and their relationship to the mechanism of the Fischer-Tropsch reaction. *J. Am. Chem. Soc.* **102**, 6181–6182 (1980).
21. Davis, B. H. Fischer-Tropsch Synthesis: reaction mechanisms for iron catalysts. *Catal. Today* **141**, 25–33 (2009).
22. Davis, B. H. Fischer-Tropsch synthesis: current mechanism and futuristic needs. *Fuel Process. Technol.* **71**, 157–166 (2001).
23. Anderson, R. B., Friedel, R. A. & Storch, H. H. Fischer-Tropsch reaction mechanism involving stepwise growth of carbon chain. *J. Chem. Phys.* **19**, 313 (1951).
24. Choi, Y. H. et al. Carbon dioxide Fischer-Tropsch synthesis: a new path to carbon-neutral fuels. *Appl. Catal. B: Environ.* **202**, 605–610 (2017).
25. Li, Z. et al. Highly selective conversion of carbon dioxide to lower olefins. *ACS Catal.* **7**, 8544–8548 (2017).
26. Bao, J., Yang, G., Yoneyama, Y. & Tsubaki, N. Significant advances in C1 catalysis: highly efficient catalysts and catalytic reactions. *ACS Catal.* **9**, 3026–3053 (2019).
27. Koeken, A. C. J. et al. Suppression of carbon deposition in the iron-catalyzed production of lower olefins from synthesis gas. *Angew. Chem. Int. Ed.* **124**, 7302–7305 (2012).
28. Ferrari, A. C. et al. Raman spectrum of graphene and graphene layers. *Phys. Rev. Lett.* **97**, 187401 (2006).
29. Espinós, J. P. et al. Interface effects for Cu, CuO, and Cu_2O deposited on SiO_2 and ZrO_2. XPS determination of the valence state of copper in Cu/SiO_2 and Cu/ZrO_2 catalysts. *J. Phys. Chem. B* **106**, 6921–6929 (2002).
30. Favaro, M. et al. Subsurface oxide plays a critical role in CO_2 activation by Cu(111) surfaces to form chemisorbed CO_2, the first step in reduction of CO_2. *Proc. Natl Acad. Sci.* **114**, 6706–6711 (2017).
31. Yang, C., Zhao, H., Hou, Y. & Ma, D. Fe_5C_2 nanoparticles: a facile bromide-induced synthesis and as an active phase for Fischer-Tropsch synthesis. *J. Am. Chem. Soc.* **134**, 15814–15821 (2012).
32. Yamashita, T. & Hayes, P. Analysis of XPS spectra of Fe^{2+} and Fe^{3+} ions in oxide materials. *Appl. Surf. Sci.* **254**, 2441–2449 (2008).
33. Song, G., Li, M., Yan, P., Nawaz, M. A. & Liu, D. High conversion to aromatics via CO_2-FT over a CO-reduced Cu-Fe_2O_3 catalyst integrated with HZSM-5. *ACS Catal.* **10**, 11268–11279 (2020).
34. Lyu, S. et al. Stabilization of ε-iron carbide as high-temperature catalyst under realistic Fischer-Tropsch synthesis conditions. *Nat. Commun.* **11**, 6219 (2020).
35. Xu, Y. et al. Highly selective olefin production from CO_2 hydrogenation on iron catalysts: a subtle synergy between manganese and sodium additives. *Angew. Chem. Int. Ed.* **59**, 21736–21744 (2020).
36. Ye, R. et al. CO_2 hydrogenation to high-value products via heterogeneous catalysis. *Nat. Commun.* **10**, 5698 (2019).

37. Liu, B. et al. Effect of supports on performance of Cu–Fe based catalysts for higher alcohols synthesis from syngas. *React. Kinet. Mech. Catal.* **128**, 695–706 (2019).

38. Mahmoudi, H. et al. A review of Fischer Tropsch synthesis process, mechanism, surface chemistry and catalyst formulation. *Biofuels Eng.* **2**, 11–31 (2017).

39. Pei, Y. et al. High alcohols synthesis via Fischer-Tropsch reaction at cobalt metal/carbide interface. *ACS Catal.* **5**, 3620–3624 (2015).

40. Qi, F. Combustion chemistry probed by synchrotron VUV photoionization mass spectrometry. *P. Combust. Inst.* **34**, 33–63 (2013).

41. Savee, J. D. et al. Direct observation and kinetics of a hydroperoxyalkyl radical (QOOH). *Science* **347**, 643–646 (2015).

42. Shaw, D. A. et al. A study of the absolute photoabsorption, photoionisation and photodissociation cross sections and the photoionisation quantum efficiency of carbon dioxide from the ionisation threshold to 345 Å. *Chem. Phys.* **198**, 381–396 (1995).

43. Adam, T. et al. Determination of single photon ionization cross sections for quantitative analysis of complex organic mixtures. *Anal. Bioanal. Chem.* **389**, 1941–1951 (2007).

44. Lu, Y. et al. Elucidating the copper-hägg iron carbide synergistic interactions for selective CO hydrogenation to higher alcohols. *ACS Catal.* **7**, 5500–5512 (2017).

45. Choi, Y. & Liu, P. Mechanism of ethanol synthesis from syngas on Rh(111). *J. Am. Chem. Soc.* **131**, 13054–13061 (2009).

46. Kresse, G. & Hafner, J. Ab initio molecular dynamics for liquid metals. *Phys. Rev. B* **47**, 558–561 (1993).

47. Kresse, G. & Hafner, J. Ab-initio molecular-dynamics for open-shell transition-metals. *Phys. Rev. B* **48**, 13115–13118 (1993).

48. Kresse, G. & Hafner, J. Ab initio molecular-dynamics simulation of the liquid-metal-amorphous-semiconductor transition in germanium. *Phys. Rev. B* **49**, 14251–14269 (1994).

49. Perdew, J. P., Burke, K. & Ernzerhof, M. Generalized gradient approximation made simple. *Phys. Rev. Lett.* **77**, 3865–3868 (1996).

50. Kresse, G. & Joubert, D. From ultrasoft pseudopotentials to the projector augmented-wave method. *Phys. Rev. B* **59**, 1758–1775 (1999).

Acknowledgements

Author contributions

Z.L. and W.W. equally contributed to this work. Z.L., W.W., H.L., and J.Z. designed the studies and wrote the paper. Z.L., W.W., and M.W. synthesized catalysts. Z.L., W.W., H.L., L.L., and K.F. performed catalytic tests. Z.L., X.M., and Y.C. conducted characterizations including SEM, XRD, XPS, TGA, and Mössbauer measurements. Y.W. contributed to DFT calculations. W.W., H.L., Y.P., and J.Z. conducted mechanistic measurements including TPD and SVUV-PIMS. All authors discussed the results and commented on the manuscript.

Competing interests

The authors declare no competing interests.

Additional information